Functional Thin Films on Surfaces

Orestis Vantzos, Omri Azencot, Max Wardeztky, Martin Rumpf, and Mirela Ben-Chen

Abstract—The motion of a thin viscous film of fluid on a curved surface exhibits many intricate visual phenomena, which are challenging to simulate using existing techniques. A possible alternative is to use a reduced model, involving only the temporal evolution of the mass density of the film on the surface. However, in this model, the motion is governed by a fourth-order nonlinear PDE, which involves geometric quantities such as the curvature of the underlying surface, and is therefore difficult to discretize. Inspired by a recent variational formulation for this problem on smooth surfaces, we present a corresponding model for triangle meshes. We provide a discretization for the curvature and advection operators which leads to an efficient and stable numerical scheme, requires a single sparse linear solve per time step, and exactly preserves the total volume of the fluid. We validate our method by qualitatively comparing to known results from the literature, and demonstrate various intricate effects achievable by our method, such as droplet formation, evaporation, droplets interaction and viscous fingering. Finally, we extend our method to incorporate non-linear van der Waals forcing terms which stabilize the motion of the film and allow additional effects such as pearling.

Index Terms—Computer Graphics, Three-Dimensional Graphics and Realism, Animation.

◆

1 INTRODUCTION

THE intricate motion of a viscous thin film subject to external forces, such as gravity, inspires research in physics, mathematics and computer science, among other scientific disciplines. In many scenarios the domain on which the fluid resides is curved rather than flat. The tear film on the cornea of the eye [1], the dynamics of lava flows [2] and the formation of ice on the aerofoil of an aircraft [3], are all examples related to the evolution of thin films on curved geometries. The goal of this paper is to suggest a method for simulating thin films on surfaces, which is based on *gradient flow* evolution and the *operator view* of the flow induced by tangent vector fields.

Generally, the *Navier–Stokes equations* coupled with appropriate boundary conditions are assumed to give a good approximation of the film's dynamics. However, for the flows we are interested in, these equations are considered difficult to solve numerically, especially on curved domains. Moreover, in the case of thin films we can assume an extremely small height-to-length ratio which leads to a substantial simplification through the *lubrication approximation* [4]. Namely, under the assumptions of the lubrication model, the evolution of the film's mass density is governed by a fourth-order nonlinear partial differential equation (PDE).

A natural approach to simulate thin films within this reduced model would then be to discretize the resulting PDE (e.g., [5]). Choosing such a strategy, however, one will be faced with two main challenges. First, one will need to derive a suitable set of discrete differential operators acting on discrete curved domains (e.g., triangle meshes). Then, the second task will be to construct a proper numerical time integration scheme. While any attempt to discretize general

PDEs will encounter these obstacles, in the particular case of thin films, the restriction on the time step size (see e.g., [6]) makes the usage of explicit schemes impractical. Although it is possible to use implicit schemes instead, such schemes do not guarantee in general the preservation of the underlying structure. For example, conserved quantities in the continuous setting (such as the total volume of the thin film) may become non-conserved in a discrete framework. Due to the above obstacles, direct discretization of the PDE is usually considered less attractive.

An alternative point of view is to leverage the *gradient flow* structure which is known to exist for thin film equations (see e.g., [7], [8]). In this model, the motion of the film is determined by the minimizer of a certain cost function, which is defined over the manifold of all possible densities of the film with prescribed volume. Intuitively, the cost function is minimized when the resistance of the fluid to flow due to dissipation induced by friction balances the additional forces (e.g., surface tension and gravity) that act on the film. One of the advantages of this approach is that every gradient flow has a natural time discretization which leads to a variational problem. In practice, it allows for significantly larger time steps compared to explicit numerical schemes. Furthermore, by construction, the associated energy is guaranteed to decrease at each step.

However, we still need to address the issues of modeling the underlying mass transport and the conservation of fluid volume. A reasonable choice within the gradient flow model is to minimize the cost function under an additional constraint given by the transport equation. Intuitively, the transport equation describes how the mass density is affected by the motion of the fluid through the corresponding velocity field. Recently, [9] suggested a coordinate-free approach for solving the transport equation on triangulated surfaces by representing tangent vector fields as *linear operators* on scalar functions. Their method is advantageous since it avoids the complicated integration of the fluid's motion, while ensuring the preservation of the integral of the transported quantity.

- *O. Vantzos, O. Azencot and M. Ben-Chen are with the Computer Science Department, Technion – Israel Institute of Technology, Israel*
- *M. Wardeztky is with Institute of Numerical and Applied Mathematics, University of Göttingen, Germany*
- *M. Rumpf is with the Institute of Numerical Simulation, University of Bonn, Germany*

In this work, we argue that the gradient flow model combined with the operator view of tangent vector fields leads to a robust and highly efficient simulation tool. Specifically, we consider the thin film model of [8] in the presence of a *precursor layer* (i.e., the film resides on top of a very thin layer defined over the whole domain) and in the geometric setting of triangulated surfaces. Under the assumption that we are given an approximate normal field, we present formulations of discrete curvature operators which are tailored for our model. In addition, we employ insights from [9] to advect the mass function of the thin film in a manner which causes very little numerical dissipation, and is guaranteed to conserve exactly the total volume of the fluid. The resulting method boils down to a *linear* solve of a sparse system per time step. We demonstrate the effects of curvature, gravity (see e.g., Fig. 1) and material parameters on the flow, and qualitatively compare our results to previous numerical simulations. Finally, we present various effects (e.g., droplet formation and interaction) which are achievable within our framework.

1.1 Related Work

As the behaviour of viscous thin films on surfaces has not, to the best of our knowledge, been previously simulated in the graphics community, we focus our attention on Eulerian methods from the computational fluid dynamics community, and to work on similar phenomena which appeared in the computer graphics literature.

The evolution of thin films over arbitrary domains has been an active area of research in CFD for many decades. We refer the interested reader to the seminal review by [10] and to the more recent review by [11]. These reviews present a continuous model for thin films, based on *lubrication theory*, which defines a reduced model for the 3D Navier–Stokes equations given the assumption of a small thickness of the film.

One approach to thin film simulation is to directly discretize the governing PDE as was shown for planar (see e.g., [12], [13]) and curved (see e.g., [5]) domains. In general, this point of view leads to several challenges, of which the restriction on the time step size for explicit schemes is perhaps the most problematic. Namely, the application of a CFL-type condition leads to the requirement that the time step τ is on the order of $(\delta x)^4$, where δx is the minimal edge length. To overcome this constraint, [6] employed convexity splitting for their time integration scheme (within a level-set framework). Nevertheless, their scheme does not guarantee conservation of the fluid's volume, and has additional restrictions due to the level-set formulation.

An alternative discretization for thin films can be derived from the gradient flow model, for which a natural variational time integrator exists. In general, variational integrators are known to conserve the underlying structure, e.g., the variational scheme in [14] preserves a notion of discrete momentum. For the case of thin films over curved domains (see e.g., [8], [15]), the gradient flow approach leads to an attractive numerical scheme. In the latter work, which is closest to our approach, the authors used Discrete Exterior Calculus (DEC) [16] for the spatial discretization, representing the flux field with discrete 1-forms. Our approach differs from their work as we use a velocity based formulation, leverage [9] for the advection, and suggest discrete curvature operators. These changes allow us to generate stable simulations on meshes with obtuse triangles which are common in graphics. A detailed comparison with [8] is given in Sections 2 and 4.

We conclude with some representative related work from the graphics community literature. Free surface flows for highly viscous fluids were suggested in [17], where effects such as melting wax are demonstrated. While one could consider adding a surface as a solid boundary and using a similar approach for simulating viscous films, it would be quite difficult to achieve the intricate effects we show without using a very dense grid resolution. More recently, various methods were proposed for modeling thin features in free surface flows by explicitly tracking the free surface mesh [18], [19], by using thickened triangle meshes [20], tetrahedral elements [21], or simplicial complexes [22], to mention just a few. Such approaches, however, require careful manipulation of the connectivity and topology of the free surface geometry, which are avoidable when simulating films on surfaces, as the free surface can be represented as a scalar function.

Finally, some approaches simulate water related phenomena. [23] model the contact angle with the surface, representing the free surface with a level-set based distance field. While various effects are achievable with this approach, the method requires a high-resolution grid which leads to a time-consuming system requiring a few days of computation per simulation. On the other hand, using a height field based method as in [24] considerably reduces computational complexity, however, the instabilities and effects we demonstrate below were not shown there.
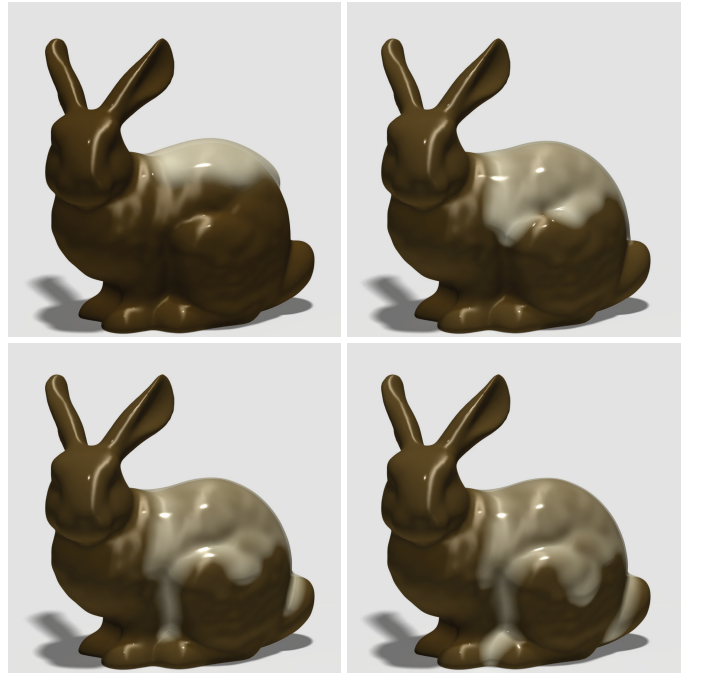

Fig. 1. Vanilla sauce on a chocolate bunny. The physical parameters are $\mathfrak{b} = 20, \epsilon = 0.1, \beta = 0$.

1.2 Contributions

Our main contributions can be described as follows:

- A discrete model for thin film evolution on *general* triangle meshes.
- An efficient and robust scheme, which exactly preserves the total fluid's volume.
- Simulation of various intricate effects, such as fingering, evaporation and droplet formation, interaction between droplets and pearling.

2 DYNAMICS OF THIN FILMS

We investigate the evolution of a layer of an incompressible viscous fluid flowing with velocity v on top of a curved surface Γ, under the influence of surface tension and, potentially, gravity. The liquid layer is attached to the surface at the liquid-solid interface, i.e., no-slip boundary condition (we extend this later), whereas the liquid-air surface is evolving freely. A typical scenario is illustrated in Figure 2 showing the notation for various related quantities.

Navier–Stokes equations. A common approach for modeling the evolution of thin liquid films is to consider the *Navier–Stokes equations*. These equations describe the fluid's velocity in the liquid phase (the *bulk*), the surface tension on the liquid-air interface (i.e., the *free surface*), and a suitable boundary condition for the velocity in the liquid-solid interface (i.e., on the solid surface). Formally, the fluid velocity v and the pressure p satisfy the equations:

$$\partial_t v + (v \cdot \nabla)v - \mu \Delta v + \nabla p = 0 \text{ in the bulk}$$
$$\operatorname{div} v = 0 \text{ in the bulk}$$
$$v = 0 \text{ on the surface} \tag{1}$$
$$\sigma n - \gamma \mathcal{H} n = 0 \text{ at the free surface}$$

where $\sigma = -p \operatorname{id} + \mu(\nabla v + \nabla v^T)$ is the stress tensor, μ and γ are the viscosity and the capillary constants (see Fig. 2). Furthermore, the free surface χ itself evolves according to the kinematic condition $\partial_t \chi = v$.

Unfortunately, a straightforward discretization of these equations is challenging. In particular, to achieve the type of effects we show below, the main obstacle is due to the prohibitively small time steps which are imposed by such a method. Moreover, the spatial discretization is also challenging since Eulerian methods will require dense sampling of the domain, whereas Lagrangian techniques will involve complex tracking of the free surface. Therefore, direct discretization of equations (1) is not practical for graphics applications for this type of problems.

Lubrication approximation. Since we are interested in *thin* films, a reduction in dimensionality can be achieved by using the *lubrication approximation* model (see e.g., [10]). In this model, the dynamics of the film are governed by the evolution of a function (i.e., a scalar quantity) defined on the surface Γ.

Given a characteristic scaling of height and length, the key assumption to consider is a small height to length ratio, i.e., $\epsilon = \frac{\text{height}}{\text{length}} \ll 1$. Then, one takes into account an asymptotic expansion of the Navier–Stokes equations with respect to ϵ, where the resulting thin film equations
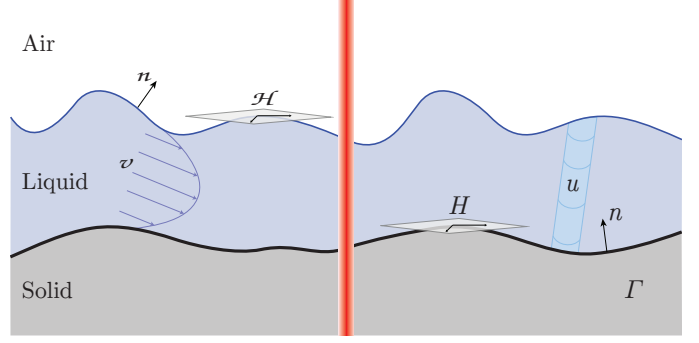

Fig. 2. A typical scenario is illustrated for the full 3D Navier–Stokes (left) compared to the reduced lubrication model (right). Notice that under the lubrication assumptions the involved quantities are computed directly on Γ, e.g., u is a scalar function.

are composed of the leading order terms. Taking this path, a derivation of a lubrication model without gravity for the *mass density* u on curved domains yields equations of the form (see [5] and [8]):

$$\partial_t u = \operatorname{div}_\Gamma \left(M(u) \nabla_\Gamma p \right) \tag{2a}$$
$$M(u) = \frac{1}{3} u^3 \operatorname{id} + \frac{\epsilon}{6} u^4 (H \operatorname{id} - S) \tag{2b}$$
$$p = -H - \epsilon T u - \epsilon \Delta_\Gamma u \tag{2c}$$

where $M(u)$ is the mobility tensor (to be discussed later) and p can be considered as a pressure-like quantity on the surface, i.e., the fluid moves away from areas of high p. H and K are the mean and Gaussian curvatures, $T = H^2 - 2K$, and S is the shape operator.

Notice that inertia effects are neglected in this model, i.e., the Reynolds number is assumed to be small, $\operatorname{Re} \ll 1$, as expected (by simple scaling arguments) for a thin enough film. Moreover, we assume that the mass density u is a proper function. As u is closely related to the fluid's height h, that is $u = h - \frac{\epsilon}{2} H h^2$, the consequence of the former constraint is that the free surface is assumed to be representable as a height function over Γ, and hence, e.g., contact angles higher than $\pi/2$ and wave-like structures cannot be modeled with equations (2).

In addition to providing a reduced model for the Navier–Stokes equations, the thin films equations are also instrumental for analyzing the behavior of the flow. As mentioned above, the fluid flows towards low pressure areas thus visualizing p allows to evaluate the underlying dynamics of the film. Moreover, a qualitative study of the expected flow can be done by estimating the different scales of the various components in p. For instance, the dominating term in Eq. (2c) is the mean curvature and hence the dynamics on curved domains are expected to be completely different when compared to the flat case (where $H = 0$). Indeed, we demonstrate this and other effects in the following example.

In Figure 3 we show the color coding of the pressure computed for an initial uniform deposition of liquid on a bumpy plane (left) and on the Scherk surface (right). These figures suggest that the fluid is most likely to accumulate at the center of the respective surfaces, where the pressure is low. Indeed, we show in Figure 4 (top) the color coding of the evolution of the mass density u on the bumpy plane, starting from a uniform layer of fluid. In this case, since the
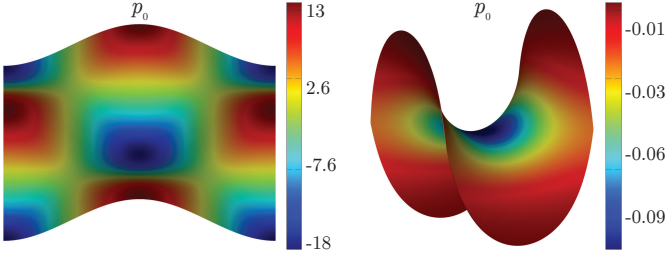
Fig. 3. By visualizing the pressure we can identify regions where the fluid is likely to accumulate. For example, for an initially uniform layer of fluid, the initial pressure p_0 indicates that fluid is expected to concentrate at the respective centers, where the pressure is lowest. See Fig. 4 for the temporal evolution of the flow.

Fig. 4. (top) The motion of the film primarily depends on the mean curvature thus the fluid concentrates in the center basin, $u_0 = 0.1, \epsilon = 0.1$. (bottom) For minimal surfaces (i.e., when $H = 0$) the film is mostly influenced by the Gaussian curvature as shown for the Scherk's surface, $u_0 = 0.1, \epsilon = 1$.

dominating term is H (top, left), the film flows towards the maximal mean curvature, at the center of the basin. Similarly, for a minimal surface, namely when $H = 0$, the terms that govern the dynamics are the Gaussian curvature and the Laplacian of u. In Figure 4 (bottom), we show frames of the flow on the Scherk minimal surface, starting again from a uniform layer of fluid. Here, the initial Laplacian of u is 0 thus the minimal Gaussian curvature (bottom, left) drives the fluid towards the center of the surface.

Unfortunately, the simulation of thin film flow based on a PDE of the form (2) suffers from serious drawbacks. First, explicit discretization of equation (2) requires very strong time step restrictions, and stable (semi-)implicit discretizations allowing for large time steps, are unknown. Second, qualitative properties, such as volume preservation and energy decay, are difficult to ensure. Finally, on general triangulated surfaces it is unclear how to discretize the geometric quantities in a physically consistent way.

These issues motivate a different approach—instead of directly discretizing the PDE, it is possible to model the evolution from the *variational* perspective of gradient flows, as was first suggested in [8]. To introduce the concepts to the graphics community, and to keep the paper self contained, we first briefly describe the gradient flow model of thin films, and then discuss our modifications in the next section.

Gradient flow model. The key insight behind the variational approach is that the quantity p can be viewed as the negative (Fréchet) derivative of the *free energy functional* $\mathcal{E}^\epsilon(u) = \int_\Gamma \left\{ -Hu - \frac{\epsilon}{2}Tu^2 + \frac{\epsilon}{2}|\nabla_\Gamma u|^2 \right\} dx$ so that the PDE (2) is of the *gradient flow* form $\partial_t u = -G(\frac{\delta \mathcal{E}^\epsilon(u)}{\delta u})$. The evolution of u then can be understood as a "steepest" descent for the free energy $\mathcal{E}^\epsilon$, at a rate regulated by the *mobility* $M(u)$ via the function $G(\phi) = \text{div}_\Gamma (M(u)\nabla_\Gamma \phi)$. The previous statement can be made precise by introducing the flux $f = -M(u)\nabla_\Gamma p$, so that the PDE can be written in the form of a flow equation as

$$\partial_t u = - \text{div}_\Gamma f. \qquad (3)$$

Then the gradient flow is equivalent to the statement that the free energy decays as $\frac{d}{dt}\mathcal{E}^\epsilon(u) = -\mathcal{D}_u^\epsilon(f, f) \leq 0$, where the bilinear form $\mathcal{D}_u^\epsilon(f, f) = \int_\Gamma f \cdot M(u)^{-1} f \, dx$ is known as the (viscous) *dissipation*. This in turn is equivalent to the variational requirement that the density variation $\partial_t u$ and
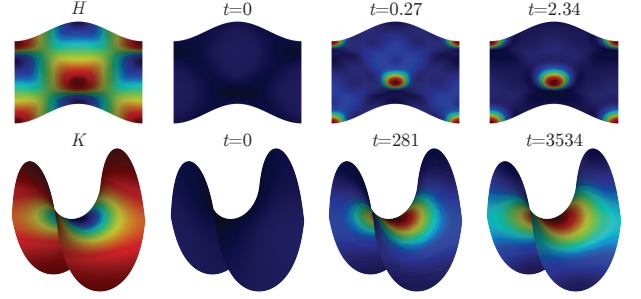
the flux f minimize (at each time t) the so-called Rayleigh functional $\frac{1}{2}\mathcal{D}_u^\epsilon(f, f) + \frac{\delta \mathcal{E}^\epsilon(u)}{\delta u}(\partial_t u)$ under the transport constraint (3).

Intuitively, the energy is an approximation of the area of the free surface, which should be minimized due to surface tension, and the dissipation is the "price to pay" for the total shear stress due to the flow inside the film. Hence, among all the possible flows which preserve the mass of the fluid, we look for the one which optimally minimizes the area of the free surface and the stress inside the film.

Finally, following the idea of *natural time discretization* of gradient flows [25] and *minimizing movements* [26], we integrate in time to arrive at a variational approximation of $u^{k+1} = u(t^k + \tau)$ given $u^k = u(t^k)$:

$$u^{k+1} = \underset{u = \mathcal{F}_\tau(u^k, f)}{\text{argmin}} \left\{ \frac{1}{2\tau}\mathcal{D}_u^\epsilon(f, f) + \mathcal{E}^\epsilon(u) \right\} \qquad (4)$$

where $\mathcal{F}_\tau(u^k, f)$ denotes a suitable (approximate) solution at $t^k + \tau$ of the initial value transport problem (3) with $u(t^k) = u^k$. The constrained minimization problem (4) is equivalent to discretizing the original PDE (2) in time; instead of the PDE then, one can describe (and discretize) the thin film flow through the three components of the gradient flow: the free energy $\mathcal{E}^\epsilon$, the dissipation $\mathcal{D}$ and the flow equation (3) (or in the time-discrete setting the flow operator $\mathcal{F}_\tau$).

In [8], suitable energy and dissipation functionals are derived for gravity- and surface tension-driven thin film flow on a *smooth* curved surface. The variational time discretization (4) is coupled then with a spatial discretization based on Discrete Exterior Calculus, resulting in a fully discrete scheme on triangulated surfaces that addresses some of the shortcomings of PDE-based solvers pointed out previously. Specifically, discrete qualitative properties are straightforward to preserve: the energy decay is built into the time discretization (4), as will be shown later, and it is also easier to set up discrete mass conservation for the flow equation than for the full PDE (2). In addition, because of the explicit control on the energy decay, the variational scheme is very stable, allowing for large time steps.

Unfortunately, directly applying that scheme for graphics purposes on *general* triangle meshes is challenging since curvature quantities and mass preserving transport are more difficult to discretize in this setting. In [8] mass preservation was achieved by working with a flux-based

formulation, that lends itself naturally to a finite-volume approach such as Discrete Exterior Calculus. However, in the presence of obtuse triangles, i.e., triangles with angles larger than $\pi/2$, negative entries can arise in the diagonal matrices that the scheme uses to define inner products between discrete k-forms. This can lead to non-convexity and eventually to instability and/or non-convergence of the variational scheme. Notice that for general meshes, eliminating these obtuse triangles is highly non-trivial.

In the next section we present our approach for discretizing the thin film gradient flow model on general triangulated surfaces. We first develop the discrete energy and dissipation terms by modeling the fluid as a prismatic layer formed by an offset surface to the triangle mesh, which naturally introduces discrete curvature quantities. In addition, we switch to a velocity-based formulation of the transport equation $\partial_t u + \mathrm{div}_\Gamma(uv) = 0$, which allows us to use the new discretization suggested in [9], that does not suffer from the aforementioned problem.

3 THIN FILMS ON TRIANGULATED SURFACES

As we have previously seen in Figure 4, the film dynamics are heavily dependent on the curvature operators, H, K and S. In their work [8] presented one dimensional applications and simulations on two dimensional surfaces where the curvatures are easy to compute analytically (such as surfaces of revolution and graphs). One could, of course, extend their method to triangulated surfaces by choosing a set of discrete curvature operators from the many available in the literature (see e.g., [27]). We chose instead to go back to fluid mechanics and look for a definition of the energy and dissipation functionals that could be applied on continuous but non-smooth surfaces, such as a triangulated mesh. We present the resulting model in this section, but have reserved a more technical derivation for the supplemental material.

Our main observation is that if Γ is equipped with a continuous vector field n that is *approximately* normal, one can follow similar derivations as in [8], and arrive at energy and dissipation functionals given by (up to an $\mathrm{O}(\epsilon^2)$ error):

$$\mathcal{E}^\epsilon(u) = \int_\Gamma (\mathfrak{b}z - H)u + \frac{\epsilon}{2}(\mathfrak{b}\cos\theta - T)u^2 + \frac{\epsilon}{2}|\nabla_\Gamma u|^2 \, da \tag{5}$$

and

$$\mathcal{D}^\epsilon_u(v, v) = \int_\Gamma v \cdot M(u)^{-1} v \, da \tag{6}$$

$$M(u) = \left(\beta + \frac{u}{3}\right)\mathrm{id} + \epsilon\frac{u^2}{12}\left(7H\,\mathrm{id} - 3S - 5\bar{S}\right) \tag{7}$$

respectively, where (unlike in [8]) the curvature quantities in these equations are now given in terms of the approximate normal field n. In (5) we included the gravity terms that involve the Bond number $\mathfrak{b}$, which measures the relative strength of gravity vs. surface tension, the altitude z, and the angle θ of the surface normal with the vertical direction. The discrete total curvature T and shape operator S are given in section 3.1 and the rotated shape operator $\bar{S}$ is given in section 3.3. Moreover, we incorporated in (7) a constant β which allows for various slip conditions.
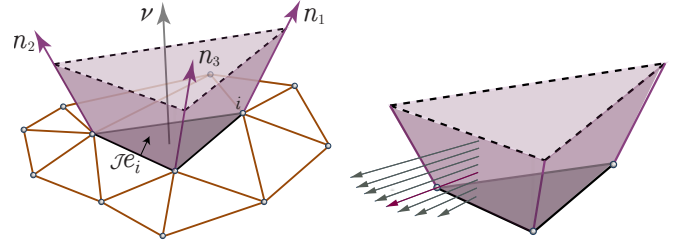

Fig. 5. (left) Prismatic layer of viscous fluid, depicted as a piecewise linear field over a triangle. (right) Prismatic volume with tangential vector field v (red) and attached Hagen-Poiseuille type velocity profile $\Pi_s(v)$.

3.1 Geometry of thin films on triangulated surfaces

For a smooth surface, the geometry of a liquid layer is modeled by a scalar height function h, which describes the extension of the liquid along a *surface normal direction* at each surface point. In the limit of thin films, this height field is scaled by a global scaling parameter ϵ. Then, the liquid layer is bounded by the surface on one side and by an offset along the surface normal by ϵh on the other. The laws of physical motion of the liquid are expressed by expanding the 3D motion up to second powers in ϵ.

Adopting this perspective for the case of a triangulated surface Γ, we take the approach of associating surface normals n as well as the offset function h with vertices and extending the resulting offset field linearly across triangles, leading to a prismatic liquid layer per triangle, see Figure 5 (left). This approach ensures continuity of the offset field across edges, which we harness to ensure mass conservation when the liquid evolves.

There is, however, a caveat with this approach: it is widely accepted that there exist no "best" vertex normals in the discrete case. Consequently, we only require *consistent* normals in the following sense. If the average edge length of the mesh is δx, it suffices that we are provided with a set of (unit length) vertex normals n such that the difference $|\nu - n|$, between the normal ν of any (flat) triangle of the mesh and the vertex normal n of its vertices, is of order δx^2. [1]

As in the smooth case, the lubrication approximation requires an additional scaling variable ϵ in which the relevant physical terms are developed up to second order. With the lateral extension of the film being measured in direction of the discrete normal n, we obtain the free surface

$$\Gamma_{\epsilon h} = \{x + \epsilon h(x)n(x) \,|\, x \in \Gamma\}$$

of the thin film at the liquid-gas interface and the fluid volume $V_{\epsilon h} = \{x + s\epsilon h(x)n(x) \,|\, x \in \Gamma, \, s \in (0, 1]\}$.

In order to derive the variational time discretization of the evolution of the thin film we make use of three different expansion formulas, namely the expansion of volume, area, and length with respect to the thickness parameter ϵ. Returning to the smooth case for a moment, such an expansion leads to expressions in terms of curvatures of the underlying surface, containing the shape operator S, its trace, and its determinant, known as mean and Gauss curvature, respectively [28].

---

1. Notice that this condition implies that $\nabla_\Gamma n$ is both tangential and symmetric up to order δx.

We exactly recover this geometric description in our discrete model. Indeed, first recall that in the smooth setting the shape operator is defined as the tangential gradient of the (smooth) unit normal field. Accordingly, we define in the discrete case a *generalized* shape operator (in the sense of considering arbitrary "normals" n) by

$$S := -\frac{1}{2} P(\nabla_\Gamma n + (\nabla_\Gamma n)^T) P \,, \tag{8}$$

where $\nabla_\Gamma = P \nabla_{\mathbb{R}^3}$ is the (triangle-based) tangential gradient on Γ and $P = \mathrm{id} - \nu \otimes \nu$ is the projection onto the (triangle-based) tangent space. From this shape operator we deduce a discrete mean curvature $H = \mathrm{Tr}(S)$ and a discrete Gaussian curvature $K = \frac{1}{2}\left(\mathrm{Tr}(S)^2 - \mathrm{Tr}(S^2)\right)$. Notice that in this setup S, and therefore also H and K, are constant per face.

Second recall that in the smooth case, mean and Gaussian curvatures *alternatively* arise by considering first and second variations of offset volume and surface area. The same holds true in the discrete case, i.e., for our prismatic layer. For example, for *the expansion of offset volume* we obtain (up to an $\mathrm{O}(\epsilon^3 + \delta x)$ error)

$$\int_{V_{\epsilon h}} \mathrm{d}x = \int_\Gamma \left(\epsilon h - \frac{\epsilon^2}{2} H h^2\right) \mathrm{d}a \,.$$

Here H equals the trace of our generalized shape operator S defined above. Hence, the two alternative *discrete* definitions of mean curvature (as the trace of the tangential gradient of the normal, and through the second order expansion of the of the offset volume) are consistent. Intuitively, the correction term $\frac{\epsilon^2}{2} H h^2$, and in particular the appearance of mean curvature, accounts for change of surface area in the lateral direction.

Notice that the integrand can be written as ϵu, with $u = h - \frac{\epsilon}{2} H h^2$. Thus u describes (up to a factor of ϵ) the *fluid volume per surface area* and can be considered as the local mass density. This quantity is an alternative and, from the viewpoint of the underlying conservation law, preferable variable.

Likewise, for *the expansion of the surface area* we obtain (up to an $\mathrm{O}(\epsilon^3 + \delta x)$ error) that

$$\int_{\Gamma_{\epsilon h}} \mathrm{d}a = \int_\Gamma \left(1 - \epsilon h H + \frac{\epsilon^2}{2}\left(2h^2 K + |\nabla_\Gamma h|^2\right)\right) \mathrm{d}a \,.$$

Notice that when $h = 1$, i.e., when one considers constant offsets, then this expression is equal to the famous Steiner formula, known from differential geometry [29]. As before, H and K that arise from the expansion of the surface area are exactly the mean and Gaussian curvatures, respectively, defined using our generalized shape operator S.

3.2 Energy

The first ingredient of our variational time discretization is the energy of the thin film, given by the sum of surface energy (the total area of the free surface $\Gamma_{\epsilon h}$, which tends to be minimized due to surface tension) and gravitational energy (weighted by the Bond number $\mathfrak{b}$):

$$\mathcal{E}(h) = \int_{\Gamma_{\epsilon h}} \mathrm{d}a + \mathfrak{b} \int_{V_{\epsilon h}} z \, \mathrm{d}x \,.$$

Here the Cartesian coordinate z denotes the altitude, i.e., we assume that gravity is acting along the z-direction.

The surface energy was spelled out above. Analogously to the expansion of the offset volume, we obtain for *the expansion of gravitational energy* (up to an $\mathrm{O}(\epsilon^3 + \delta x)$ error) that

$$\int_{V_{\epsilon h}} z \, \mathrm{d}V = \int_\Gamma \left(\epsilon z h + \frac{\epsilon^2}{2}\left(-h^2 H z + h^2 \cos\theta\right)\right) \mathrm{d}a \,.$$

Here, per triangle, θ is the angle of the direction of gravity with the triangle normal. Exchanging the height h against the mass density u and restricting to the (non constant) leading order terms we finally end up with the energy functional

$$\mathcal{E}^\epsilon(u) = \int_\Gamma (\mathfrak{b} z - H)u + \frac{\epsilon}{2}\left(\mathfrak{b}\cos\theta - T\right)u^2 + \frac{\epsilon}{2}|\nabla_\Gamma u|^2 \mathrm{d}a \tag{9}$$

with $T = H^2 - 2K$.

3.3 Conservation law for the flow

Mass conservation during the temporal evolution of the fluid is one of the central physical principles of viscous flow [30]. Violations of this principle in numerical simulations lead to undesirable artefacts. For our approach, we outline how mass conservation can be *exactly* maintained by working with a conservation law in *divergence* form. Mass conservation is a balance principle: the change of volume must equal the flux of material across the volume boundary. On an arbitrary (triangular) patch T this translates into the balance equation

$$\frac{\mathrm{d}}{\mathrm{d}t} \int_{V_{\epsilon h}(T)} \mathrm{d}x = \int_{F_{\epsilon h}(T)} \mathfrak{v} \cdot \mu \, \mathrm{d}a \,,$$

where $\mathfrak{v}$ is the fluid's velocity vector and μ is the (inward pointing) normal of the faces $F_{\epsilon h}(T)$ of the prism $V_{\epsilon h}(T)$ above T (cf. Fig. 5 (right)). Using the divergence theorem of Gauss and Taylor expansions in the height, which corresponds to an expansion of the length functional on the edges of the patch, we obtain the conservation law

$$\partial_t u = -\mathrm{div}_\Gamma \left(u \int_0^\epsilon Q_s \mathfrak{v}_{\Gamma,s} \, \mathrm{d}s\right) \,,$$

where $\mathfrak{v}_{\Gamma,s}(x)$ is the tangential component of the velocity in the liquid layer and the tensor $Q_s = \mathrm{id} - s u \left(\bar{S} - H\,\mathrm{id}\right)$ accounts for the geometry of the prism $V_{\epsilon h}(T)$. The rotated shape operator $\bar{S} = -[\nu]_\times S [\nu]_\times$ is defined via the skew-symmetric matrix $[\nu]_\times$, which in turn is given by requiring that $[\nu]_\times \cdot x = \nu \times x$ for any vector x. We define the (weighted) average velocity $v = \int_0^\epsilon Q_s \mathfrak{v}_{\Gamma,s} \, \mathrm{d}s$, independent of s, so that the conservation law is restricted to the triangulated surface Γ and takes the simple form

$$\partial_t u + \mathrm{div}_\Gamma(u\,v) = 0 \,. \tag{10}$$

The weighting reflects the inclination and torsion of the faces of the prisms. The advantage of working with an averaged velocity is that it resides directly on the surface Γ. In the discrete case, this velocity field can be modeled using piecewise constant (per triangle) vector fields, and mass balance can be expressed using commonly used discrete differential operators.

3.4 Dissipation and mobility

In the previous section, we used averaging in order to reduce the velocity field in the bulk to a velocity field on the surface. For treating dissipation, we require the opposite direction, i.e., to reconstruct a velocity field in the bulk from the velocity filed on the surface. Since the inverse of averaging allows for many solutions, this reconstruction step is not unique a priori. In order to single out a unique velocity field in the bulk, we invoke a physical principle by considering the field that causes least energy dissipation.

Concretely, we require a (tensor) profile function Π_s such that $\mathfrak{v}_{\Gamma,s} = \Pi_s v$ and $\int_0^\epsilon Q_s \Pi_s \, \mathrm{d}s = \mathrm{id}$ (see Fig. 5 (right)). Note that there are many possible velocity profiles $\Pi : s \mapsto \Pi_s$ that satisfy this integral constraint. From the theory of viscous flows [31] we know that the physically observed profile minimizes the viscous dissipation rate $\int_{V_{\epsilon_h}} |\nabla \mathfrak{v} + \nabla \mathfrak{v}^T|^2 \, \mathrm{d}x$. This is dominated by the vertical shear stress, i.e., the normal derivative of the tangential velocity, which can be expressed as a quadratic form in $\mathfrak{v}$. Approximating this quadratic form to leading order in ϵ, substituting $\mathfrak{v}$ by $\Pi(v)$, and optimizing the transportation cost for given boundary conditions $\Pi_0 = 0$ (no-slip at substrate) and zero shear stress at free surface under the integral constraint $\int_0^\epsilon Q_s \Pi_s \, \mathrm{d}s = \mathrm{id}$, yields an optimal profile Π^*, which to leading order matches the well-known Hagen-Poiseuille profile. We thus obtain the dissipation as a function of the averaged velocity v as

$$\mathcal{D}_u^\epsilon(v,v) = \int_\Gamma v \cdot M(u)^{-1} v \, \mathrm{d}a, \qquad (11)$$

where the mobility tensor is defined as

$$M(u) = \frac{u}{3} + \epsilon \frac{u^2}{12} \left(7H \, \mathrm{id} - 3S - 5\bar{S}\right).$$

For a more detailed derivation of the optimal profile see the supplemental material.

3.5 Minimizing movement approach

Combining the three building blocks we have derived, and using the minimizing movement approach, we arrive at an effective variational time discretization for the evolution of a thin film on a triangulated surface. The energy $\mathcal{E}^\epsilon$ (9) depends on the mass density u, whereas the dissipation $\mathcal{D}_u^\epsilon$ (11) is a quadratic form on motion fields v. For given u^k at time step k any mass density u at time step $k+1$ results from the transport of u^k via an underlying motion field. Hence, the time discrete conservation law (10) has to be handled as a constraint representing the coupling of u and v. Altogether, we iteratively define u^{k+1} as the minimizer u of the following constrained optimization problem:

$$\min_{u,v} \left\{ \frac{1}{2\tau} \mathcal{D}_{u^k}^\epsilon(v,v) + \mathcal{E}^\epsilon(u) \right\}$$
$$\text{subject to } u = T_\tau(v)(u^k),$$

where $T_\tau(v)$ denotes the operation of transporting u^k with constant velocity v for a time interval of length τ. The factor $\frac{1}{2\tau}$ reflects the proper rescaling in time to obtain the dissipation to be spent to transform u^k into u.

We consider a number of extensions to this model, which are known for the flat case [10]. The first one replaces on Γ the no-slip $v = 0$ by the *Navier slip condition* $v = \beta \partial_n v$ with β denoting the slip length (in case of large variation of the velocity in the normal direction, the fluid undergoes slipping on the surface Γ). To reflect this one has to add β to the mobility M. This slip boundary conditions accelerates the motion of the fluid. Furthermore, we consider *evaporation*. It takes the form of a sink term in the right hand side of the conservation law and is modeled in the time discrete setup by the constraint $u - T_\tau(v)(u^k) = -\frac{u}{(u^k + c_e)^2}$, for a small constant c_e. Intuitively, the evaporation rate is faster for thinner films, which reflects a faster heating of thinner films.

4 SPATIAL DISCRETIZATION

The main challenge here is to define a stable discretization of the transport equation (10) such that various properties (e.g., energy decay and mass preservation) will hold on general triangle meshes. While many of the operators we use are standard in geometry processing, we highlight the properties these operators should possess such that the resulting optimization scheme would indeed be stable.

Notation. We consider a triangle mesh and denote by $\mathcal{V}$ its vertex set and by $\mathcal{F}$ its face set. We use bold faced symbols to denote the spatial discrete analogues of continuous quantities (e.g., $\boldsymbol{u}$ is the discrete mass density). When required, we use the subscripts $\mathcal{V}$ and $\mathcal{F}$ to denote quantities on the vertices and the faces, respectively. The bracket $[\cdot]$ operator is used to convert vectors in $\mathbb{R}^{|\mathcal{V}|}$ and $\mathbb{R}^{|\mathcal{F}|}$ to block diagonal matrices in $\mathbb{R}^{|\mathcal{V}| \times |\mathcal{V}|}$ and $\mathbb{R}^{3|\mathcal{F}| \times 3|\mathcal{F}|}$ respectively (replicating each entry 3 times for the latter).

Functions, vector fields and inner products. We use a typical setup, i.e., piecewise-linear functions and piecewise-constant vector fields, with corresponding inner products. Specifically, we represent real-valued functions as scalars on the vertices of the mesh, i.e., $\boldsymbol{u} \in \mathbb{R}^{|\mathcal{V}|}$, and extend them to the whole mesh using piecewise linear hat basis functions. Similarly, vector fields are treated as piecewise-constant on the faces of the mesh, i.e., $\boldsymbol{v} \in \mathbb{R}^{3|\mathcal{F}|}$.

For defining discrete inner products we require vertex and face areas, denoted by $\boldsymbol{A}_\mathcal{V} \in \mathbb{R}^{|\mathcal{V}|}$ and $\boldsymbol{A}_\mathcal{F} \in \mathbb{R}^{|\mathcal{F}|}$, respectively. For the vertex area we use $1/3$ of the total area of its adjacent triangles, and we define an interpolating matrix $\boldsymbol{I}_\mathcal{V}^\mathcal{F} \in \mathbb{R}^{|\mathcal{V}| \times |\mathcal{F}|}$ which interpolates quantities from faces to the vertices, i.e., $\boldsymbol{I}_\mathcal{V}^\mathcal{F}(i,j) = \frac{\boldsymbol{A}_\mathcal{F}(j)}{3\boldsymbol{A}_\mathcal{V}(i)}$, iff vertex i belongs to face j and 0 otherwise. This choice implies that $\boldsymbol{A}_\mathcal{F} = (\boldsymbol{I}_\mathcal{V}^\mathcal{F})^T \boldsymbol{A}_\mathcal{V}$, which will be important for consistency later. Now, discrete inner products are defined by:

$$\int_\Gamma \boldsymbol{u_1} \boldsymbol{u_2} \mathrm{d}a = \boldsymbol{u_1}^T \boldsymbol{G}_\mathcal{V} \boldsymbol{u_2}, \quad \int_\Gamma \langle \boldsymbol{v_1}, \boldsymbol{v_2} \rangle \mathrm{d}a = \boldsymbol{v_1}^T \boldsymbol{G}_\mathcal{F} \boldsymbol{v_2},$$

where $\boldsymbol{G}_\mathcal{V} = [\boldsymbol{A}_\mathcal{V}] \in \mathbb{R}^{|\mathcal{V}| \times |\mathcal{V}|}$ and $\boldsymbol{G}_\mathcal{F} = [\boldsymbol{A}_\mathcal{F}] \in \mathbb{R}^{3|\mathcal{F}| \times 3|\mathcal{F}|}$ denote the diagonal mass matrix of the vertices and the faces.

Differential Operators. Equations (5) and (10) require discrete gradient and divergence operators. In the smooth case, these operators fulfill integration by parts, namely on a surface without boundary we have: $\int_\Gamma \langle v, \nabla_\Gamma u \rangle \, \mathrm{d}a + \int_\Gamma u \cdot \mathrm{div}_\Gamma v \, \mathrm{d}a = 0$. In order to maintain discrete preservation of mass (see appendix A), we need the operators

$\mathbf{grad}_\Gamma \in \mathbb{R}^{3|\mathcal{F}|\times|\mathcal{V}|}$ and $\mathbf{div}_\Gamma \in \mathbb{R}^{|\mathcal{V}|\times 3|\mathcal{F}|}$ to fulfill this discretely, namely:

$$\boldsymbol{v}^T \boldsymbol{G}_\mathcal{F}(\mathbf{grad}_\Gamma \boldsymbol{u}) + (\mathbf{div}_\Gamma \boldsymbol{v})^T \boldsymbol{G}_\mathcal{V}\boldsymbol{u} = 0,$$

for arbitrary $\boldsymbol{v}$ and $\boldsymbol{u}$. Interestingly, the standard operators (e.g., as defined in [32, Chapter 3]) fulfill this property.

Approximate normal field, curvature and gravity. As described in the previous section, all of the required curvature quantities can be computed once a suitable approximate normal field is given. In practice, we use the area-weighted averages of triangle normals [32, pg. 42] as vertex normals. By applying the discrete gradient operator defined previously, the tangential gradient of the discrete normal field per face j is:

$$(\nabla_\Gamma \boldsymbol{n})_j = \frac{1}{2\boldsymbol{A}_\mathcal{F}(j)} \left(\sum_{i=1}^{3} \boldsymbol{n}_{j_i}(\mathcal{J}\boldsymbol{e}_{j_i})^T \right)$$

where the sum runs over the three vertex normals $\boldsymbol{n}_{j_i}$ of the face and $\mathcal{J}\boldsymbol{e}_{j_i}$ is the rotated (by $\pi/2$) edge opposite to vertex i in the triangle j (see Figure 5). The gravity quantities can be computed as follows: $\boldsymbol{z}$ is the vertical coordinate function and $\cos\boldsymbol{\theta}$ is the vertical component function of $\boldsymbol{n}$.

Mobility. The discrete mobility $\boldsymbol{M}(\boldsymbol{u})$ is a $3|\mathcal{F}| \times 3|\mathcal{F}|$ *diagonal* matrix, where for each face the associated quantities can be computed using Eq. (7), the curvature operators, and the interpolated mass density $\boldsymbol{u}_\mathcal{F}$ on the faces ($\boldsymbol{u}$ is defined on vertices).

Transport operator. In the continuous case, equation (10) guarantees that the integral of $\partial_t u$ vanishes on a closed surface (since the divergence of any vector field integrates to 0). However, once we discretize u and v then $\mathbf{div}_\Gamma(\boldsymbol{uv})$ is no longer well defined using our discrete operators, since $\boldsymbol{uv}$ is not a piecewise constant vector field. To avoid this issue, we first apply the product rule to (10) and reformulate the constraint as $\partial_t u = -(v \cdot \nabla_\Gamma u + u \, \mathrm{div}_\Gamma v)$. We then follow [9] and define a directional derivative $\boldsymbol{D}(\boldsymbol{v})$ such that $\mathbf{1}_\mathcal{V}^T \boldsymbol{G}_\mathcal{V} \left(\boldsymbol{D}(\boldsymbol{v}) + [\mathbf{div}_\Gamma \boldsymbol{v}] \right) \boldsymbol{u} = 0$ for any $\boldsymbol{u}$ and $\boldsymbol{v}$ (see appendix A for the proof). Specifically, the directional derivative is given as $\boldsymbol{D}(\boldsymbol{v}) \in \mathbb{R}^{|\mathcal{V}|\times|\mathcal{V}|}$ by $\boldsymbol{D}(\boldsymbol{v}) = \boldsymbol{I}_\mathcal{V}^\mathcal{F}[\boldsymbol{v}]_\bullet^T \, \mathbf{grad}_\Gamma$, where $[\cdot]_\bullet \in \mathbb{R}^{3|\mathcal{F}|\times3|\mathcal{F}|}$ converts vector fields to block diagonal matrices.

The main advantage of this point of view is that in the discrete case the transport equation turns into a system of ODEs of the form $\partial_t \boldsymbol{u} + \boldsymbol{A}\boldsymbol{u} = 0$, for a constant matrix $\boldsymbol{A}$, which can be solved using a matrix exponential [33]. Thus, for a velocity $\boldsymbol{v}$ constant in time, the discrete transport equation can be solved in the time interval $[t^k, t^k + \tau]$ to yield the solution

$$\boldsymbol{u} = \exp\left(-\tau\boldsymbol{D}(\boldsymbol{v}) - \tau[\mathbf{div}_\Gamma \boldsymbol{v}]\right) \boldsymbol{u}^k \qquad (12)$$

at $t = t^k + \tau$, where τ is the time step. In the case of evaporation, we have an additional term $-\tau[\boldsymbol{u}^k + c_e]^{-2}$ in the exponential.

We compared our transport scheme to the method of [8] on the bunny model which has obtuse triangles. Specifically, we computed the difference in energy and the minimal u in the first iteration for different time step sizes. In Figure 6 (left) we show that our method is consistently decreasing

the energy, whereas the method of [8] actually increases the energy for small time steps. In addition, we show in Figure 6 (right) that their method yields negative values for u even for very small time steps, whereas ours preserves the initial value of the precursor layer.
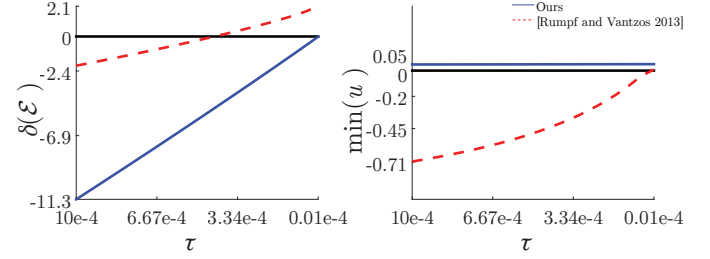

Fig. 6. Comparison with [8]. (left) Plot of the observed energy reduction $\delta(\mathcal{E}) = \mathcal{E}(t + \tau) - \mathcal{E}(t)$ as a function of the time step τ, on a mesh with obtuse triangles. The present scheme consistently decreases the energy ($\delta(\mathcal{E}) \leq 0$), whereas the other method has trouble with small time steps. (right) Regarding the positivity of the solution, again on a mesh with obtuse triangles, the present method preserves the initial minimum u, whereas the other method exhibits negative values of u.

Furthermore, the suggested transport mechanism is more appropriate to the flows we are interested in than the one suggested by [8]. In particular, droplet formation and fingering instabilities are transport-dominated effects. Thus, a natural requirement from a transport mechanism is to exhibit minimum diffusion, allowing to capture better resolved fingers on relatively coarse meshes as we demonstrate. We show in Figure 7 that starting from the same initial conditions, our scheme is qualitatively less diffusive compared to the method of [8].

5 FULLY DISCRETE MODEL

Given the above discrete operators and quantities, we can write the fully-discrete optimization problem for computing $\boldsymbol{u}, \boldsymbol{v}$ given $\boldsymbol{u}^k$:

$$\min_{\boldsymbol{u},\boldsymbol{v}} \left\{ \frac{1}{2\tau} \mathcal{D}_{\boldsymbol{u}^k}^\epsilon(\boldsymbol{v},\boldsymbol{v}) + \mathcal{E}^\epsilon(\boldsymbol{u}) \right\}, \qquad (13)$$

subject to $\boldsymbol{u} = \exp\left(-\tau\boldsymbol{D}(\boldsymbol{v}) - \tau[\mathbf{div}_\Gamma \boldsymbol{v}]\right) \boldsymbol{u}^k$.
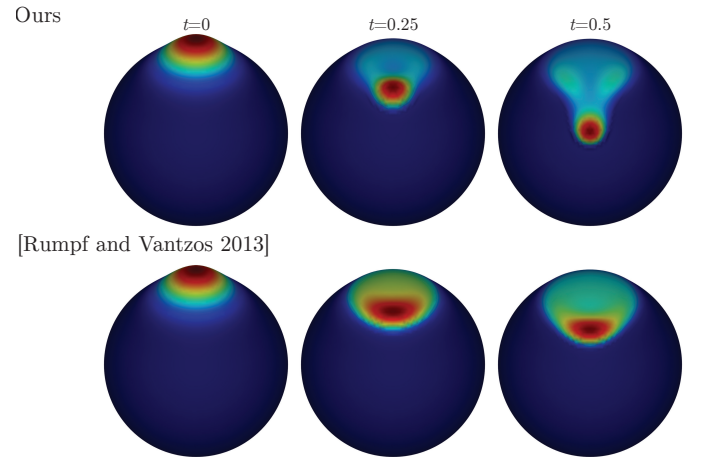

Fig. 7. Starting from the same initial conditions and physical parameters, our transport scheme (top) achieves a better resolved finger compared to the result (bottom) generated with the more diffusive scheme suggested in [8].

Then, the fully-discrete energy and dissipation are given by:

$$\mathcal{E}^{\epsilon}(\boldsymbol{u}) = \boldsymbol{a}^T \boldsymbol{G}_{\mathcal{V}} \boldsymbol{u} + \frac{\epsilon}{2} \boldsymbol{u}^T (\boldsymbol{G}_{\mathcal{V}} \boldsymbol{B} + \boldsymbol{L}) \boldsymbol{u},$$

$$\mathcal{D}^{\epsilon}_{\boldsymbol{u}^k}(\boldsymbol{v}, \boldsymbol{v}) = \boldsymbol{v}^T \boldsymbol{G}_{\mathcal{F}} \boldsymbol{M}(\boldsymbol{u}^k)^{-1} \boldsymbol{v},$$

where $\boldsymbol{a} = \mathfrak{b}\boldsymbol{z} - \boldsymbol{H}$, $\boldsymbol{B} = \mathfrak{b}\cos\theta - \boldsymbol{H}^2 + 2\boldsymbol{K}$, and the stiffness matrix $\boldsymbol{L} = -\boldsymbol{G}_{\mathcal{V}} \operatorname{div}_{\Gamma} \operatorname{grad}_{\Gamma}$.

5.1 Properties

Discrete energy. *The discrete energy* $\mathcal{E}^{\epsilon}(\boldsymbol{u}^k)$ *is non increasing.*

Proof: Noticing that $\boldsymbol{u} = \boldsymbol{u}^k$ and $\boldsymbol{v} = 0$ is an admissible pair for the minimization problem (13) since they satisfy the constraint, we have immediately that:

$$\frac{1}{2\tau}\mathcal{D}^{\epsilon}_{\boldsymbol{u}^k}(\boldsymbol{v}^{k+1}, \boldsymbol{v}^{k+1}) + \mathcal{E}^{\epsilon}(\boldsymbol{u}^{k+1}) \leq \frac{1}{2\tau}\mathcal{D}^{\epsilon}_{\boldsymbol{u}^k}(0, 0) + \mathcal{E}^{\epsilon}(\boldsymbol{u}^k)$$
$$\Rightarrow \mathcal{E}^{\epsilon}(\boldsymbol{u}^{k+1}) \leq \mathcal{E}^{\epsilon}(\boldsymbol{u}^k)$$

since $\mathcal{D}^{\epsilon}_{\boldsymbol{u}^k}(\boldsymbol{v}^{k+1}, \boldsymbol{v}^{k+1}) \geq 0$ and $\mathcal{D}^{\epsilon}_{\boldsymbol{u}^k}(0, 0) = 0$.

Intuitively, since $\mathcal{D}$ is non-negative, if the fluid moved and "paid" with dissipation, then it found a smaller energy solution (otherwise it will have remained at the previous state, with the same energy).

Discrete mass. *The total discrete mass* $m(\boldsymbol{u}) = \int_{\Gamma} \boldsymbol{u} \, \mathrm{d}a = \mathbf{1}_{\mathcal{V}}^T \boldsymbol{G}_{\mathcal{V}} \boldsymbol{u}$ *is exactly preserved.*

Proof: The transport equation (12) can be written as $\boldsymbol{u} = \exp(-\tau\boldsymbol{A})\boldsymbol{u}^k$, where $\boldsymbol{A} = \boldsymbol{D}(\boldsymbol{v}) + [\operatorname{div}_{\Gamma} \boldsymbol{v}]$. In appendix A we show $\mathbf{1}_{\mathcal{V}}^T \boldsymbol{G}_{\mathcal{V}} \boldsymbol{A} = 0$ for any velocity $\boldsymbol{v}$. Hence, we have $m(\boldsymbol{u}^k) - m(\boldsymbol{u}) = \mathbf{1}_{\mathcal{V}}^T \boldsymbol{G}_{\mathcal{V}} \{\mathrm{id} - \exp(-\tau\boldsymbol{A})\} \boldsymbol{u}^k = \mathbf{1}_{\mathcal{V}}^T \boldsymbol{G}_{\mathcal{V}} \left\{ \tau\boldsymbol{A} - \frac{\tau^2}{2}\boldsymbol{A}^2 + \dots \right\} \boldsymbol{u}^k = 0$.

5.2 Optimization

To solve the discrete variational model (13) we use the first order approximation $\exp(-\tau\boldsymbol{A}) \approx \mathrm{id} - \tau\boldsymbol{A}$ of the matrix exponential, so that the linear equation:

$$\boldsymbol{u} = \boldsymbol{u}^k - \tau(\boldsymbol{D}(\boldsymbol{v}) + [\operatorname{div}_{\Gamma} \boldsymbol{v}])\boldsymbol{u}^k \tag{14}$$

replaces the non-linear constraint (12). Hence, at every time step we solve *a quadratic problem with a linear constraint*, which is convex for a small enough τ (see §5.3 "Dynamic Time-stepping"). As we will show next, this can be done very efficiently, by solving a single linear system for $\boldsymbol{u}$. Note that it is straightforward to check that the results of §5.1 hold for the linearized constraint as well, hence we gain efficiency yet do not lose stability.

The linear system. Using the method of Lagrange multipliers we obtain the *first order necessary conditions*:

$$\boldsymbol{G}_{\mathcal{F}} \boldsymbol{M}(\boldsymbol{u}^k)^{-1} \boldsymbol{v} - \left(\overline{\boldsymbol{D}}(\boldsymbol{u}^k) + [\boldsymbol{u}^k] \operatorname{div}_{\Gamma} \right)^T \boldsymbol{G}_{\mathcal{V}} \boldsymbol{p} = 0$$

$$\boldsymbol{G}_{\mathcal{V}}(\boldsymbol{a} + \epsilon\boldsymbol{B}\boldsymbol{u}) + \epsilon\boldsymbol{L}\boldsymbol{u} - \boldsymbol{G}_{\mathcal{V}}\boldsymbol{p} = 0 \tag{15}$$

$$\boldsymbol{G}_{\mathcal{V}}\left(\boldsymbol{u} - \boldsymbol{u}^k + \tau(\boldsymbol{D}(\boldsymbol{v}) + [\operatorname{div}_{\Gamma} \boldsymbol{v}])\boldsymbol{u}^k \right) = 0,$$

where $\boldsymbol{p}$ is the dual variable.

A key ingredient to deriving (15) is the *dual operator* $\overline{\boldsymbol{D}}(\boldsymbol{u})$, defined such that $\boldsymbol{D}(\boldsymbol{v})\boldsymbol{u} = \overline{\boldsymbol{D}}(\boldsymbol{u})\boldsymbol{v}$, as it allows us to take derivatives with respect to $\boldsymbol{v}$. This operator is: $\overline{\boldsymbol{D}}(\boldsymbol{u}) = \boldsymbol{I}_{\mathcal{V}}^{\mathcal{F}}[\operatorname{grad}_{\Gamma} \boldsymbol{u}]_{\bullet}^T$. Similarly, it holds that $([\boldsymbol{u}] \operatorname{div}_{\Gamma}) \boldsymbol{v} = [\operatorname{div}_{\Gamma} \boldsymbol{v}]\boldsymbol{u}$.

Figure	$|\mathcal{V}|$	Avg. per step	#steps	Total time
Fig. 1, Bunny*	38306	0.484	1999	967.8
Fig. 4, Bumpy plane	40401	0.683	4996	3410.4
Fig. 4, Scherk surface	40401	0.627	1997	1252.4
Fig. 9, Rounded cube*	19728	0.142	4991	709.5
Fig. 10, Sphere	40962	1.645	300	493.5
Fig. 12, Moomoo*	16710	0.080	1981	158.4
Fig. 13, Torus	40000	1.079	456	491.8
Fig. 14, Moai	89126	3.106	314	975.3
Fig. 15, Rain	10242	0.198	18001	3570.1
Fig. 17, Pensatore	27732	0.818	991	810.3
Fig. 16, Wine glass*	38976	0.708	496	351.1

TABLE 1
Timing statistics (in seconds). Asterisk denotes simulations where an iterative solver was used, whereas for the rest, we used a direct non-iterative solver.

Finally, eliminating $\boldsymbol{v}$ and $\boldsymbol{p}$, we arrive at the following *reduced linear system* for $\boldsymbol{u}$:

$$\left(\mathrm{id} + \tau\epsilon\, \boldsymbol{R}(\boldsymbol{u}^k, \boldsymbol{u}_e^k)(\boldsymbol{G}_{\mathcal{V}}\boldsymbol{B} + \boldsymbol{L}) \right)\boldsymbol{u} = \boldsymbol{u}_e^k - \tau\boldsymbol{R}(\boldsymbol{u}^k, \boldsymbol{u}_e^k)\boldsymbol{G}_{\mathcal{V}}\boldsymbol{a} \tag{16}$$

where $\boldsymbol{R}(\boldsymbol{u}^k, \boldsymbol{u}_e^k) = \boldsymbol{F}(\boldsymbol{u}_e^k)\boldsymbol{M}(\boldsymbol{u}^k)\boldsymbol{G}_{\mathcal{F}}^{-1}\boldsymbol{F}(\boldsymbol{u}_e^k)^T$ and $\boldsymbol{F}(\boldsymbol{u}_e^k) = \overline{\boldsymbol{D}}(\boldsymbol{u}_e^k) + [\boldsymbol{u}_e^k] \operatorname{div}_{\Gamma}$ and $\boldsymbol{u}_e^k = \exp(-\tau[\boldsymbol{u}^k + c_e]^{-2})\boldsymbol{u}^k$ if evaporation is included and $\boldsymbol{u}_e^k = \boldsymbol{u}^k$ otherwise.

Thus, we obtain a fully discrete scheme where given an initial mass density $\boldsymbol{u}_0$, we evolve it in time using the above update rule.

We implemented our method in MATLAB using standard linear solvers for Eq. (16). In all our experiments, the method was very stable allowing for large time steps (on the scale of $\mathrm{O}(\epsilon + \delta x)$, which is excellent for 4th order problems) depending on the initial conditions and the underlying mesh. The experiments were performed on an Intel(R) Xeon(R) processor with 32 GB RAM, and we show in Table 1 the statistics for the different simulations.

5.3 Limitations

Dynamic Time-Stepping. Given that the stiffness matrix $\boldsymbol{L}$ is positive semi-definite, the system (16) is invertible as long as $\tau_1 \epsilon\|\boldsymbol{R}(\boldsymbol{u}^k)\|_2\|\boldsymbol{G}_{\mathcal{F}}\|_2\underline{\boldsymbol{B}} \leq 1$, where $\underline{\boldsymbol{B}}$ is the absolute taken on the minimum value of $\boldsymbol{B}$ and it is a measure of how strongly negative the quantity $\mathfrak{b}\cos\theta - T$ is on the surface. Moreover, we employ a CFL-type condition depending on the maximum velocity of the film $\underline{\boldsymbol{v}}$, and grid size, i.e., we require that $\tau_2\underline{\boldsymbol{v}} \leq \delta x$. Finally, we take the time step to be $\tau = \min\{\tau_1, \tau_2\}$.

Positivity Preservation. Unfortunately, even if we start from a strictly positive $\boldsymbol{u}_0$, the evolution of the film $\boldsymbol{u}^k$ is not guaranteed to stay positive [8]. Aside from being non-physical, in the case of negative values, droplets might rupture. In practice, all of our simulations remain positive, excluding the evaporation example. Nevertheless, the evaporation term has a stabilizing effect, indeed, negative mass concentrations are also evaporated. Intuitively, positivity is difficult to maintain due to the jump in pressure along the triple line (the interface
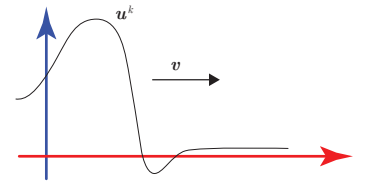

Fig. 8. Capillarity ridge with high velocity and undershooting.

where air, solid and liquid meet). Moreover, the so-called capillary ridge is formed, due to the competition between surface tension and other forcing effects, e.g., gravity, see Figure 8 and 9. Thus, right where the film is at its thinnest, the resulting velocity is high, implying instability along the direction of motion. We leave further investigation of the issue of positivity preservation for future work.
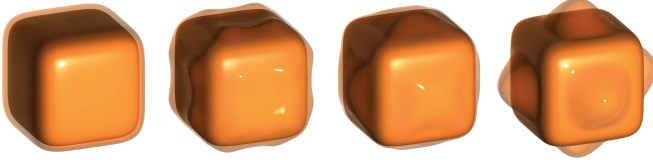

Fig. 9. In the absence of gravity, the fluid departs areas where the mean curvature is strongly negative and capillary ridges form. Later, surface tension balances the fluid on top of every face, cf. [5] ($u_0 = 0.1, \mathfrak{b} = 0, \epsilon = 0.1, \beta = 0$).

Meshes with creases. In general, the model we developed in Section 2 has a strong dependency on the consistency of the vertex normals. In practice, general meshes might have creases, or small dihedral angles, which will cause H to be arbitrarily negatively large and non-smooth. This can have a detrimental effect on the simulation, as the fluid will be drawn towards these singular locations. There are two possible remedies for this situation: we can either refine the mesh (possibly non-uniformly), however that would require additional pre-processing before one can apply our scheme to an arbitrary model. Alternatively, we can add a regularizer to the energy so that it is easier to control the simulation. We opted for the second option, as it makes our method easier to use, and can allow the artist some freedom to control the simulation in a non-physical way. Hence, for meshes with creases (see e.g., Fig. 17), we multiply the stiffness matrix L defined in Section 5 by a constant $1 \leq r \leq 100$. This effectively adds some numerical diffusion, allowing for more smooth solutions. Note that discrete conservation of mass is not affected by this modification.

Detachment of fluid. As the fluid is "tied" to the surface, droplets cannot detach when they become too large. In these cases, the droplets grow narrower and taller until equilibrium is reached and the approximate lubrication solution is stable, although the full 3D flow is not. Note, that in this case one could potentially switch to a full 3D simulation, which will allow the droplet to separate from the surface. This is an interesting direction for future research.

6 EXPERIMENTAL RESULTS

Parameter exploration. We begin by exploring the effect of various parameter choices on the simulation of the thin film. For this example, we choose a sphere as a simple geometric model with limited curvature effects on the flow. The basic experiment includes placing a concentration of fluid at the top of the sphere, with slightly perturbed initial conditions to avoid perfect symmetry. Due to gravity the fluid flows downward, and the initial perturbations give rise to fingering instabilities, (see [34] for an experimental demonstration of fingering on a sphere). The result for the

parameters $\epsilon = 0.05, \mathfrak{b} = 50, \beta = 0$ is shown in Figure 10 (f), demonstrating the emergence of a secondary finger in the center (see also Fig. 16, showing multiple fingers in a wine glass).

We refer to this setup as the *reference configuration*, and now modify in every column of the figure a single parameter to isolate its effect on the simulation, for which we show a snapshot at time $t = 10$. Left: varying $\mathfrak{b}$ changes the speed with which the film flows downward, without strongly affecting the shape of the fingers. Specifically, for a lower $\mathfrak{b}$ value (a), the secondary finger does not emerge yet, whereas for a higher $\mathfrak{b}$ value (b) it is more pronounced than in the reference configuration. Middle: changing ϵ affects the surface tension component, and therefore the shape of the fingers. Reducing ϵ yields thinner fingers (c), whereas increasing it (d) makes more viscous thick fingers, and eliminates the secondary finger. Right: increasing β considerably speeds up the fluid (e), allowing it to flow more freely in all directions (as opposed to increasing $\mathfrak{b}$ which causes faster flow in the direction of gravity).

Energy reduction. The numerical scheme we use is guaranteed by construction to reduce the energy $\mathcal{E}(\boldsymbol{u})$ at every time step. Figure 11 shows the energy decay in time, for the different simulations in Figure 10. We observe that the slip parameter β affects the speed with which the energy is reduced, the gravity parameter $\mathfrak{b}$ also affects the initial value of the energy, and the parameter ϵ has a minor impact on the energy, as it is dominated by the leading order term.

Thin films interaction. Figure 12 demonstrates the flow and interaction of thin films on the moomoo model. The higher bulk of fluid accumulates beneath the horns of the model, followed by a faster motion when it comes in contact with the lower bulk of fluid (see also Figure 14). Then, the motion is mostly determined by the two main fingers flowing on the sides of the model. In Fig. 15 we show the interaction of many droplets viewed from four sides of the unit sphere. We repeatedly pour new droplets at the top of the sphere at a fixed rate and drain the liquid from the bottom.

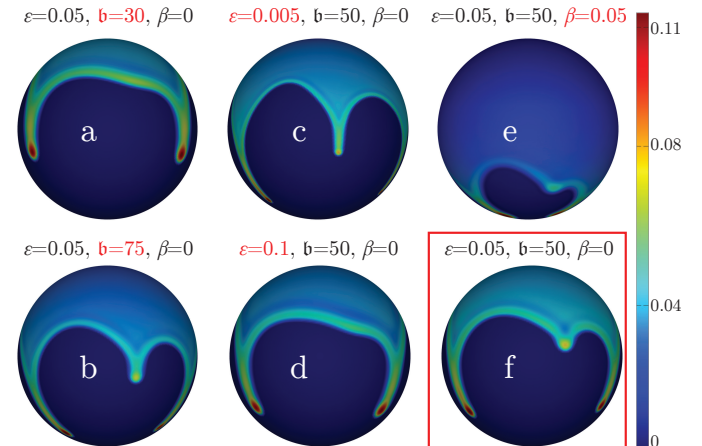**Droplet formation.** A thin film concentrating *beneath* a flat

Fig. 10. Fingering behavior for varying parameters, at $t = 10$. In every column, one parameter is modified from the reference configuration (f). See the text for details.
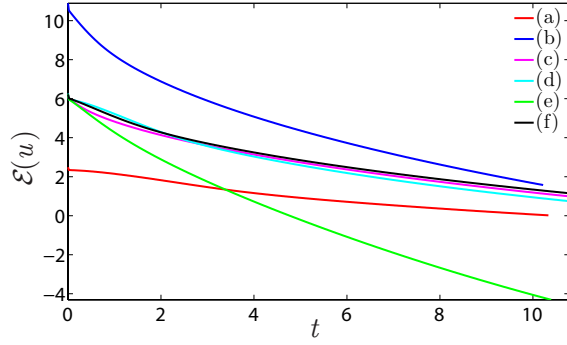
Fig. 11. The energy $\mathcal{E}(u)$ for the simulations in Figure 10.

surface develops an instability called *droplet formation* (cf. [35]). In Figure 13, we start with a uniform layer of fluid on the torus with small perturbations, and allow it to drop beneath the torus due to gravity. As the fluid accumulates around the circular set of lowest points, droplets form.

Evaporation. Figure 14 shows how evaporation ($c_e = 0.01$) and the precursor layer affect the motion of the film. We deposit precursor layers of different heights on the two halves of the Moai model and place a similar bulk of fluid near the eyes. Due to the initially thicker precursor layer, even though it evaporates quickly, the film on the left part of the model flows to a greater distance compared to the film on the right. Eventually, all the film evaporates.

7 VAN DER WAALS POTENTIAL TERM.

As mentioned in the limitations section, a major drawback of our method is that the positivity of the mass density $\boldsymbol{u}$ is *not* guaranteed. One approach towards solving this issue is to add the integrated non-linear potential term $\int_\Gamma W(u)\mathrm{d}a \approx \mathbf{1}_\mathcal{V}^T \boldsymbol{G}_\mathcal{V} \boldsymbol{W}(\boldsymbol{u})$ to the discrete energy $\mathcal{E}^\epsilon(\boldsymbol{u})$. The purpose of this term is to penalize values of $\boldsymbol{u}$ that are under a certain threshold $\boldsymbol{u_p}$. A computationally simple choice, commonly used to model intermolecular forces, is the well-known *Lennard-Jones (LJ) potential* [36] given by

$$\boldsymbol{W}(\boldsymbol{u}) = \frac{1}{2}\left(\frac{\boldsymbol{u_p}}{\boldsymbol{u}}\right)^4 - \left(\frac{\boldsymbol{u_p}}{\boldsymbol{u}}\right)^2 .$$
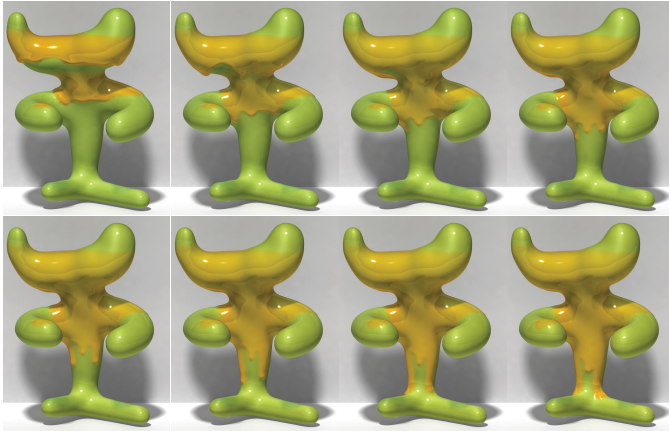

Fig. 12. Flow on the moomoo model ($\mathfrak{b} = 20, \epsilon = 0.1, \beta = 0$). Note how the upper and lower films interact: the larger mass density of the upper film causes it to catch up with the lower front leading to the formation of quickly propagating fingers.
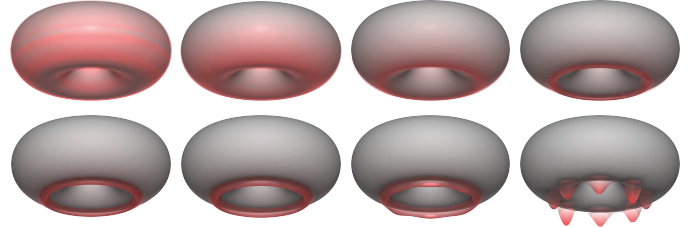

Fig. 13. Starting from a perturbed uniform layer of fluid, the fluid flows downwards, accumulates and finally forms droplets.

In the context of thin films, the LJ potential was used in [37], and in addition to maintaining the height of the precursor layer, it also leads to the spontaneous formation of droplets (*pearling*) due to the potential well (see inset figure). Namely, the modified energy favors large densities of fluid (where the potential is zero) or densities of the precursor layer size (where the potential has a minimum). Overall, using the LJ potential stabilizes the simulation by promoting the continued positivity of the solution. Although it is not entirely accurate physically, it is similar enough to the real intermolecular interactions, that occur between substrate, liquid film and the air and determine the hydrophobic/hydrophilic properties of the surface, to achieve visually appealing results.

The modifications needed to incorporate the LJ potential can be summarized as follows. The new energy is given by $\mathcal{E}_{\boldsymbol{W}}^\epsilon(\boldsymbol{u}) = \mathcal{E}^\epsilon(\boldsymbol{u}) + \mathbf{1}_\mathcal{V}^T \boldsymbol{G}_\mathcal{V} \boldsymbol{W}(\boldsymbol{u})$. Thus, the new Euler–Lagrange equations (15) can be reduced to the following primal-dual system

$$\boldsymbol{p} = \boldsymbol{a} + \epsilon\left(\boldsymbol{B} + \boldsymbol{G}_\mathcal{V}^{-1}\boldsymbol{L}\right)\boldsymbol{u} + \boldsymbol{W}'(\boldsymbol{u}) ,$$
$$\boldsymbol{u} = \boldsymbol{u}^k - \tau\boldsymbol{R}(\boldsymbol{u}^k)\boldsymbol{G}_\mathcal{V}\boldsymbol{p} . \tag{17}$$

Therefore, the resulting Newton system can be written as

$$\begin{pmatrix} \mathrm{id} & -\epsilon(\boldsymbol{B} + \boldsymbol{G}_\mathcal{V}^{-1}\boldsymbol{L}) - [\boldsymbol{W}''(\boldsymbol{u})] \\ \tau\boldsymbol{R}(\boldsymbol{u}^k)\boldsymbol{G}_\mathcal{V} & \mathrm{id} \end{pmatrix} \begin{pmatrix} \delta\boldsymbol{p} \\ \delta\boldsymbol{u} \end{pmatrix} = \begin{pmatrix} \boldsymbol{r_p} \\ \boldsymbol{r_u} \end{pmatrix} , \tag{18}$$

where

$$-\boldsymbol{r_p} = \boldsymbol{p} - \boldsymbol{a} - \epsilon(\boldsymbol{B} + \boldsymbol{G}_\mathcal{V}^{-1}\boldsymbol{L})\boldsymbol{u} - \boldsymbol{W}'(\boldsymbol{u}) ,$$
$$-\boldsymbol{r_u} = \boldsymbol{u} - \boldsymbol{u}^k + \tau\boldsymbol{R}(\boldsymbol{u}^k)\boldsymbol{G}_\mathcal{V}\boldsymbol{p} .$$

The correction for $\boldsymbol{\delta p}$ can be eliminated, resulting in a single equation for the update of $\boldsymbol{u}$. The modified update rule (16) for the correction is given by

$$\left(\mathrm{id} + \tau\,\boldsymbol{R}(\boldsymbol{u}^k)\boldsymbol{G}_\mathcal{V}\left(\epsilon(\boldsymbol{B} + \boldsymbol{G}_\mathcal{V}^{-1}\boldsymbol{L}) + [\boldsymbol{W}''(\boldsymbol{u})]\right)\right)\delta\boldsymbol{u} =$$
$$\boldsymbol{u} - \boldsymbol{u}^k + \tau\boldsymbol{R}(\boldsymbol{u}^k)\boldsymbol{G}_\mathcal{V}\left(\boldsymbol{a} + \epsilon\left(\boldsymbol{B} + \boldsymbol{G}_\mathcal{V}^{-1}\boldsymbol{L}\right)\boldsymbol{u} + \boldsymbol{W}'(\boldsymbol{u})\right) . \tag{19}$$

A single Newton step takes the form of $\boldsymbol{u} \leftarrow \boldsymbol{u} - \gamma\boldsymbol{\delta u}$, with $0 < \gamma \leq 1$ such that the energy is reduced. In practice we took $\gamma = 1$ in all of the examples that we show. As for the initial guess for the Newton iterations, we took $\boldsymbol{u} = \boldsymbol{u}^k$. Unfortunately, the concavity of $\boldsymbol{W}(\boldsymbol{u})$ poses a too strict requirement on τ for the system (19) to be invertible. In practice, we split the potential to its convex $\boldsymbol{W_+}(\boldsymbol{u})$ and
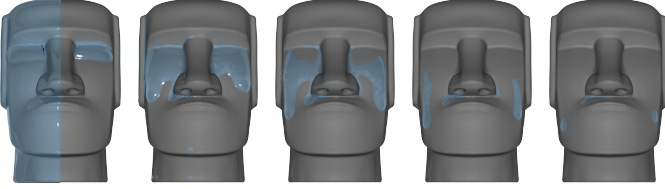
Fig. 14. Evaporation effect on the evolution of the film.

concave $-\boldsymbol{W}_-(\boldsymbol{u})$ parts, so that the usual bound discussed in subsection 5.3 can be used. Specifically, we define

$$\tilde{\boldsymbol{W}}(\boldsymbol{u}^k, \boldsymbol{u}) = \boldsymbol{W}_+(\boldsymbol{u}) - \Big(\boldsymbol{W}_-(\boldsymbol{u}^k) + \boldsymbol{W}'_-(\boldsymbol{u}^k)(\boldsymbol{u} - \boldsymbol{u}^k) \Big) \, ,$$

where for the LJ potential we have $\boldsymbol{W}_+(\boldsymbol{u}) = \frac{1}{2} \left(\frac{\boldsymbol{u}_p}{\boldsymbol{u}} \right)^4$ and $\boldsymbol{W}_-(\boldsymbol{u}) = \left(\frac{\boldsymbol{u}_p}{\boldsymbol{u}} \right)^2$. Finally, we modify the system (19) such that $\boldsymbol{W}''(\boldsymbol{u}) \to \boldsymbol{W}''_+(\boldsymbol{u})$ and $\boldsymbol{W}'(\boldsymbol{u}) \to \boldsymbol{W}'_+(\boldsymbol{u}) - \boldsymbol{W}'_-(\boldsymbol{u}^k)$. Note that a small value for the threshold $\boldsymbol{u}_p$ can approximate an effectively de-wetted surface (i.e. a very thin precursor layer) with droplets of apparently compact support. As small values of $\boldsymbol{u}_p$ exacerbate the non-convexity of the LJ potential, this necessitates smaller time steps.

In Figure 18 we show the effect of *pearling* that occurs whenever a trail of thin layer of liquid appears during the motion. In Figure 19 we show that due to the high attractive and repulsive forces, droplets emerge spontaneously. Both of these effects are achievable due to the Van der Waals nonlinear potential term.

8 CONCLUSION

We presented a novel method for simulating viscous thin film flow on triangulated meshes. Our approach is based on a variational time discretization and is therefore stable and allows for large time steps. Furthermore, we guarantee by construction that the discrete total mass is preserved and that the discrete energy is non-increasing. The algorithm is based on a single sparse linear solve per iteration, and is therefore very efficient. We demonstrated various intricate film motions, such as viscous fingering and droplet interaction.

There are many potential extensions to our model. For instance, it might be possible to extend the model to handle effects due to surface tension gradient. Also, our discretization of the mass transport constraint might be potentially useful in additional applications. Finally, we mentioned various extensions throughout the paper such as positivity preservation and fluid detachment which might be interesting to achieve.

APPENDIX
DISCRETE CONSERVATION OF MASS

To prove that mass is strictly preserved we recall the first order necessary conditions in the context of the Lagrangian.

$$\tau \boldsymbol{G}_{\mathcal{F}} \boldsymbol{M}(\boldsymbol{u}^k)^{-1} \boldsymbol{v} - \tau \left(\overline{\boldsymbol{D}}(\boldsymbol{u}^k) + [\boldsymbol{u}^k] \operatorname{\mathbf{div}}_\Gamma \right)^T \boldsymbol{G}_{\mathcal{V}} \boldsymbol{p} = 0$$

$$\boldsymbol{G}_{\mathcal{V}} (\boldsymbol{a} + \epsilon \boldsymbol{B} \boldsymbol{u}) + \epsilon \boldsymbol{L} \boldsymbol{u} - \boldsymbol{G}_{\mathcal{V}} \boldsymbol{p} = 0$$

$$\boldsymbol{G}_{\mathcal{V}} \left(\boldsymbol{u} - \boldsymbol{u}^k + \tau (\boldsymbol{D}(\boldsymbol{v}) + [\operatorname{\mathbf{div}}_\Gamma \boldsymbol{v}]) \boldsymbol{u}^k \right) = 0$$

It is interesting to note that, using the definition of $\boldsymbol{L}$ and a discrete integration by parts, the second equation is equivalent to $\boldsymbol{p} = \boldsymbol{a} + \epsilon \boldsymbol{B} \boldsymbol{u} - \epsilon \operatorname{\mathbf{div}}_\Gamma \operatorname{\mathbf{grad}}_\Gamma \boldsymbol{u}$ in correspondence to the corresponding continuous equation $p = a + \epsilon b u - \epsilon \Delta_\Gamma u$.

At first, we rewrite the first equation and get

$$\boldsymbol{v} = \boldsymbol{M}(\boldsymbol{u}^k) \boldsymbol{G}_{\mathcal{F}}^{-1} \Big(\overline{\boldsymbol{D}}(\boldsymbol{u}^k) + [\boldsymbol{u}^k] \operatorname{\mathbf{div}}_\Gamma \Big)^T \boldsymbol{G}_{\mathcal{V}} \boldsymbol{p}$$

$$= \boldsymbol{M}(\boldsymbol{u}^k) \boldsymbol{G}_{\mathcal{F}}^{-1} \Big([\operatorname{\mathbf{grad}}_\Gamma \boldsymbol{u}^k]_\bullet (\boldsymbol{I}_{\mathcal{V}}^{\mathcal{F}})^T \boldsymbol{G}_{\mathcal{V}} \boldsymbol{p} + \operatorname{\mathbf{div}}_\Gamma^T [\boldsymbol{u}^k] \boldsymbol{G}_{\mathcal{V}} \boldsymbol{p} \Big)$$

$$= \boldsymbol{M}(\boldsymbol{u}^k) \boldsymbol{G}_{\mathcal{F}}^{-1} \Big([(\boldsymbol{I}_{\mathcal{V}}^{\mathcal{F}})^T \boldsymbol{G}_{\mathcal{V}} \boldsymbol{p}] \operatorname{\mathbf{grad}}_\Gamma \boldsymbol{u}^k + \operatorname{\mathbf{div}}_\Gamma^T \boldsymbol{G}_{\mathcal{V}} [\boldsymbol{u}^k] \boldsymbol{p} \Big)$$

$$= \boldsymbol{M}(\boldsymbol{u}^k) \boldsymbol{G}_{\mathcal{F}}^{-1} \Big([\boldsymbol{G}_{\mathcal{F}} \boldsymbol{I}_{\mathcal{F}}^{\mathcal{V}} \boldsymbol{p}] \operatorname{\mathbf{grad}}_\Gamma \boldsymbol{u}^k - \boldsymbol{G}_{\mathcal{F}} \operatorname{\mathbf{grad}}_\Gamma [\boldsymbol{u}^k] \boldsymbol{p} \Big)$$

$$= \boldsymbol{M}(\boldsymbol{u}^k) \Big([\boldsymbol{p}_{\mathcal{F}}] \operatorname{\mathbf{grad}}_\Gamma \boldsymbol{u}^k - \operatorname{\mathbf{grad}}_\Gamma [\boldsymbol{u}^k] \boldsymbol{p} \Big)$$

using the facts that $\boldsymbol{G}_{\mathcal{V}}$ and $[\boldsymbol{u}^k]$ commute as diagonal matrices, that $[\boldsymbol{v}]_\bullet \boldsymbol{u}_{\mathcal{F}} = [\boldsymbol{u}_{\mathcal{F}}] \boldsymbol{v}$ for any $\boldsymbol{u}_{\mathcal{F}}$ (discrete scalar on faces) and $\boldsymbol{v}$ (discrete vector), and that the interpolation matrices are defined so that $\boldsymbol{I}_{\mathcal{F}}^{\mathcal{V}} = \boldsymbol{G}_{\mathcal{F}}^{-1} (\boldsymbol{I}_{\mathcal{V}}^{\mathcal{F}})^T \boldsymbol{G}_{\mathcal{V}}$. Again, it is interesting to note that the equation above is an approximation of the corresponding continuous one:

$$v = M(u^k) \left(p \nabla_\Gamma u^k - \nabla_\Gamma (u^k p) \right) = -u^k M(u^k) \nabla_\Gamma p$$

Now, we consider the discrete $m(\boldsymbol{u}) = \boldsymbol{1}_{\mathcal{V}}^T \boldsymbol{G}_{\mathcal{V}} \boldsymbol{u}$ with $\boldsymbol{1}_{\mathcal{V}}$ a vector of ones of length $|\mathcal{V}|$. Indeed, multiplying the third equation with $\boldsymbol{1}_{\mathcal{V}}^T$, using the duality of $\boldsymbol{D}$ and $\overline{\boldsymbol{D}}$, and taking into account that the interpolation matrix $\boldsymbol{I}_{\mathcal{F}}^{\mathcal{V}}$ is defined so that $\boldsymbol{I}_{\mathcal{F}}^{\mathcal{V}} \boldsymbol{1}_{\mathcal{V}} = \boldsymbol{1}_{\mathcal{F}}$ we obtain

$$m(\boldsymbol{u}^{k+1}) - m(\boldsymbol{u}^k) = -\tau \, \boldsymbol{1}_{\mathcal{V}}^T \boldsymbol{G}_{\mathcal{V}} \left(\boldsymbol{D}(\boldsymbol{v}) + [\operatorname{\mathbf{div}}_\Gamma \boldsymbol{v}] \right) \boldsymbol{u}^k$$

$$= -\tau \, \boldsymbol{1}_{\mathcal{V}}^T \boldsymbol{G}_{\mathcal{V}} \left(\overline{\boldsymbol{D}}(\boldsymbol{u}^k) + [\boldsymbol{u}^k] \operatorname{\mathbf{div}}_\Gamma \right) \boldsymbol{v}$$

$$= -\tau \, \boldsymbol{v}^T \left(\overline{\boldsymbol{D}}(\boldsymbol{u}^k) + [\boldsymbol{u}^k] \operatorname{\mathbf{div}}_\Gamma \right)^T \boldsymbol{G}_{\mathcal{V}} \boldsymbol{1}_{\mathcal{V}}$$

$$= -\tau \, \boldsymbol{v}^T \boldsymbol{G}_{\mathcal{F}} \left([\boldsymbol{I}_{\mathcal{F}}^{\mathcal{V}} \boldsymbol{1}_{\mathcal{V}}] \operatorname{\mathbf{grad}}_\Gamma \boldsymbol{u}^k - \operatorname{\mathbf{grad}}_\Gamma [\boldsymbol{u}^k] \boldsymbol{1}_{\mathcal{V}} \right)$$

$$= -\tau \, \boldsymbol{v}^T \boldsymbol{G}_{\mathcal{F}} \left(\operatorname{\mathbf{grad}}_\Gamma \boldsymbol{u}^k - \operatorname{\mathbf{grad}}_\Gamma \boldsymbol{u}^k \right) = 0 \, .$$
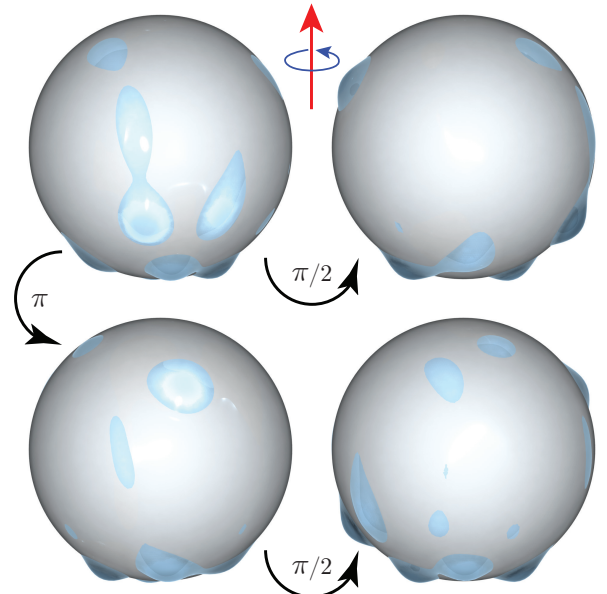

Fig. 15. Rain of droplets lead to their interesting interaction over the sphere (see the video for the full simulation). The sphere is shown from its four sides, where the axis of rotation is shown above.

The key step is applying the previous calculation with $p = \mathbf{1}_\mathcal{V}$ and so *the discrete conservation of mass is equivalent to the fact that a constant discrete pressure gives zero discrete velocity.*

REFERENCES

[1] R. Braun, R. Usha, G. McFadden, T. Driscoll, L. Cook, and P. King-Smith, "Thin film dynamics on a prolate spheroid with application to the cornea," *J. of Eng. Math.*, vol. 73, no. 1, pp. 121–138, 2012.

[2] R. Griffiths, "The dynamics of lava flows," *Ann. Rev. of Fluid Mechanics*, vol. 32, no. 1, pp. 477–518, 2000.

[3] T. G. Myers and J. P. Charpin, "A mathematical model for atmospheric ice accretion and water flow on a cold surface," *Int. J. of Heat and Mass Transfer*, vol. 47, no. 25, pp. 5483–5500, 2004.

[4] O. Reynolds, "On the theory of lubrication and its application to Mr. Beauchamp tower's experiments, including an experimental determination of the viscosity of olive oil." *Proc. of the Royal Society of London*, vol. 177, pp. 157–234, 1886.

[5] R. V. Roy, A. J. Roberts, and M. Simpson, "A lubrication model of coating flows over a curved substrate in space," *J. of Fluid Mechanics*, vol. 454, pp. 235–261, 2002.

[6] J. B. Greer, A. L. Bertozzi, and G. Sapiro, "Fourth order partial differential equations on general geometries," *J. of Comp. Physics*, vol. 216, no. 1, pp. 216–246, 2006.

[7] L. Giacomelli and F. Otto, "Rigorous lubrication approximation," *Interfaces and Free boundaries*, vol. 5, no. 4, pp. 483–530, 2003.

[8] M. Rumpf and O. Vantzos, "Numerical gradient flow discretization of viscous thin films on curved geometries," *Math. Models and Methods in Applied Sciences*, vol. 23, no. 05, pp. 917–947, 2013.

[9] O. Azencot, M. Ben-Chen, F. Chazal, and M. Ovsjanikov, "An operator approach to tangent vector field processing," in *CGF*, vol. 32, no. 5. Wiley Online Library, 2013, pp. 73–82.

[10] A. Oron, S. H. Davis, and S. G. Bankoff, "Long-scale evolution of thin liquid films," *Rev. of modern physics*, vol. 69, no. 3, p. 931, 1997.

[11] R. Craster and O. Matar, "Dynamics and stability of thin liquid films," *Reviews of modern physics*, vol. 81, no. 3, p. 1131, 2009.

[12] L. Zhornitskaya and A. L. Bertozzi, "Positivity-preserving numerical schemes for lubrication-type equations," *SIAM J. on Numerical Analysis*, vol. 37, no. 2, pp. 523–555, 1999.

[13] G. Grün and M. Rumpf, "Nonnegativity preserving convergent schemes for the thin film equation," *Numerische Mathematik*, vol. 87, no. 1, pp. 113–152, 2000.

[14] P. Mullen, K. Crane, D. Pavlov, Y. Tong, and M. Desbrun, "Energy-preserving integrators for fluid animation," *ACM Trans. Graph.*, vol. 28, no. 3, p. 38, 2009.

[15] O. Vantzos, "Thin viscous films on curved geometries," Ph.D. dissertation, Universitäts-und Landesbibliothek Bonn, 2014.

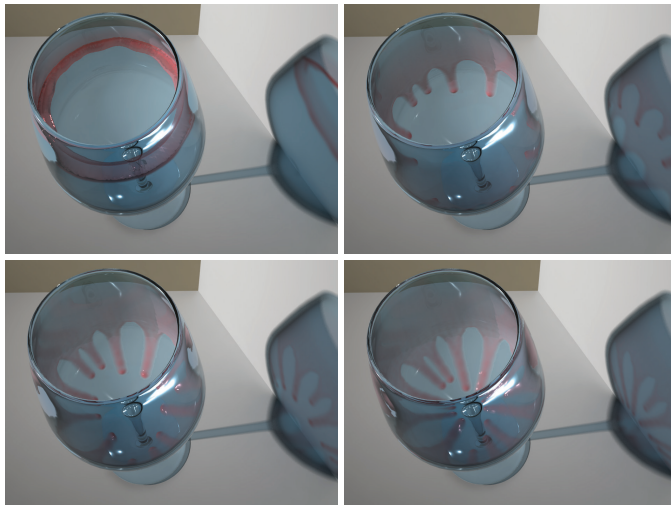[16] A. N. Hirani, "Discrete exterior calculus," Ph.D. dissertation, California Institute of Technology, 2003.

[17] M. Carlson, P. J. Mucha, R. B. Van Horn III, and G. Turk, "Melting and flowing," in *Proc. of SCA 2002*, 2002, pp. 167–174.

[18] C. Wojtan, M. Müller-Fischer, and T. Brochu, "Liquid simulation with mesh-based surface tracking," in *ACM SIGGRAPH 2011 Courses*. ACM, 2011.

[19] Y. Zhang, H. Wang, S. Wang, Y. Tong, and K. Zhou, "A deformable surface model for real-time water drop animation," *Vis. and Comp. Graph., IEEE Trans. on*, vol. 18, no. 8, 2012.

[20] C. Batty, A. Uribe, B. Audoly, and E. Grinspun, "Discrete viscous sheets," *ACM Trans. Graph.*, vol. 31, no. 4, p. 113, 2012.

[21] P. Clausen, M. Wicke, J. R. Shewchuk, and J. F. O'brien, "Simulating liquids and solid-liquid interactions with lagrangian meshes," *ACM Trans. Graph.*, vol. 32, no. 2, p. 17, 2013.

[22] B. Zhu, E. Quigley, M. Cong, J. Solomon, and R. Fedkiw, "Codimensional surface tension flow on simplicial complexes," *ACM Trans. Graph.*, vol. 33, no. 4, p. 111, 2014.

[23] H. Wang, P. J. Mucha, and G. Turk, "Water drops on surfaces," *ACM Trans. Graph.*, vol. 24, no. 3, pp. 921–929, 2005.

[24] H. Wang, G. Miller, and G. Turk, "Solving general shallow wave equations on surfaces," in *Proc. of SCA 2007*, 2007, pp. 229–238.

[25] F. Otto, "The geometry of dissipative evolution equations: the porous medium equation," *Comm. in Partial Differential Equations*, vol. 26, no. 1-2, pp. 101–174, 2001.
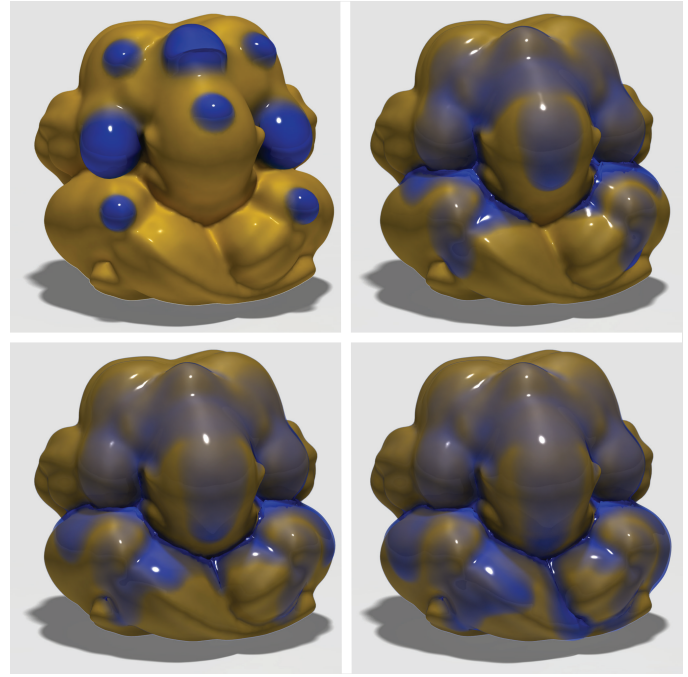
Fig. 17. Thin film flow on a geometrically complicated model. Note how starting from a few blobs of fluid, the film naturally follows the creases of the object, merges and splits accordingly.

Fig. 16. Multiple fingers on the inside of a glass of wine ($\mathfrak{b} = 500, \epsilon = 0.0001, \beta = 0$).
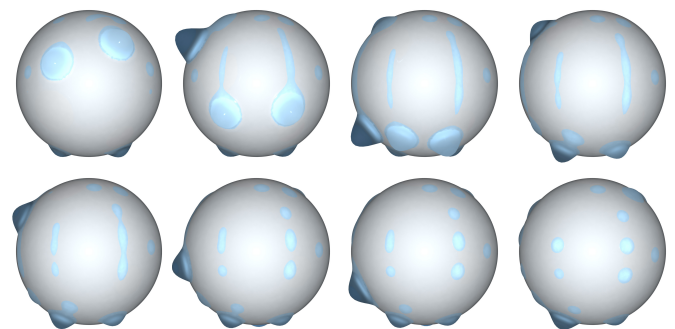

Fig. 18. The two big droplets (top, left) travel fast enough to leave a trail of fluid behind (top, middle and right), which later separates into several smaller droplets (bottom). This phenomenon is known as *pearling*.

[26] E. Giorgi and L. Ambrosio, "New problems on minimizing movements," in *Ennio De Giorgi selected papers*. Springer, 2006, pp. 699–714.

[27] T. D. Gatzke and C. M. Grimm, "Estimating curvature on triangular meshes," *Int. J. of shape modeling*, vol. 12, no. 01, pp. 1–28, 2006.

[28] M. P. Do Carmo, *Differential geometry of curves and surfaces*. Prentice-Hall Englewood Cliffs, 1976, vol. 2.

[29] H. Federer, *Geometric measure theory*. Springer New York, 1969, vol. 1996.

[30] A. J. Chorin and J. E. Marsden, *A mathematical introduction to fluid mechanics*. Springer, 1990, vol. 3.

[31] C. Pozrikidis, *Introduction to theoretical and computational fluid dynamics*. Oxford University Press, 2011.

[32] M. Botsch, L. Kobbelt, M. Pauly, P. Alliez, and B. Lévy, *Polygon mesh processing*. CRC press, 2010.

[33] M. Hochbruck and A. Ostermann, "Exponential integrators," *Acta Numerica*, vol. 19, pp. 209–286, 2010.

[34] D. Takagi and H. E. Huppert, "Flow and instability of thin films on a cylinder and sphere," *J. of Fluid Mech.*, vol. 647, p. 221, 2010.

[35] A. Sharma and R. Khanna, "Pattern formation in unstable thin liquid films," *Phys. Rev. Lett.*, vol. 81, pp. 3463–3466, Oct 1998. [Online]. Available: http://link.aps.org/doi/10.1103/PhysRevLett.81.3463

[36] J. E. Jones, "On the determination of molecular fields. ii. from the equation of state of a gas," in *Proceedings of the Royal Society of London A: Mathematical, Physical and Engineering Sciences*, vol. 106, no. 738. The Royal Society, 1924, pp. 463–477.

[37] G. Grün and M. Rumpf, "Simulation of singularities and instabilities arising in thin film flow," *European Journal of Applied Mathematics*, vol. 12, no. 03, pp. 293–320, 2001.
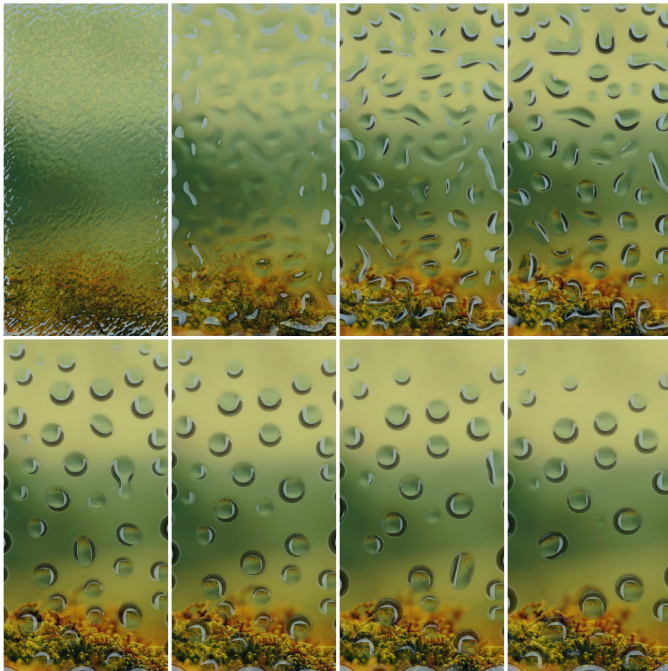
Fig. 19. Starting from a slightly perturbed uniform layer of fluid (top, left), droplets quickly form due to the attractive/repulsive forces resulting from the van der Waals non-linear potential (top, middle and right). Later, the droplets travel downwards due to gravity and several merges between droplets occur (bottom).